Cenozoic Pb–Zn–Ag mineralization in the Western Alps

maxime bertauts, Adrien Vezinet, Emilie Janots, Magali Rossi, Isabelle Duhamel-Achin, Philippe Lach, Pierre Lanari

Cenozoic Pb–Zn–Ag mineralization in the Western Alps

Maxime Bertauts[1], Adrien Vezinet[1], Emilie Janots[1], Magali Rossi[2], Isabelle Duhamel-Achin[3],

Philippe Lach[4] and Pierre Lanari[5]

[1]Univ. Grenoble Alpes, Univ. Savoie Mont Blanc, CNRS, IRD, Univ. Gustave Eiffel, ISTerre,

38000 Grenoble, France

[2]Univ. Grenoble Alpes, Univ. Savoie Mont-Blanc, CNRS, EDYTEM, 73000 Chambéry, France

[3]BRGM, F-13276 Marseille, France

[4]BRGM, F-45060 Orléans, France

[5]Institut für Geologie, Universität Bern, 3012 Bern, Switzerland

ABSTRACT

Metallogenic models of polyphase mountain belts critically rely on robust geochronology. We combine petrology with Rb–Sr and U–Th–Pb in situ geochronology, paired at thin-section scale, to date mineralization in deformed hydrothermal Pb–Zn–Ag deposits along an east-west transect in the Western Alps, France. The Pb–Zn–Ag veins occur in shear zones with kinematic structures consistent with the mylonitized host rocks. The ore consists mainly of galena in a quartz-phengite gangue. The paragenesis can be related to hydrothermal crystallization during periods of variable strain. Both isotope systems yield only Cenozoic ages (ca. 35 Ma and 15–20 Ma) without any pre-Alpine inheritance, clearly indicating orogenic mineralization. The metallogenic model proposed here includes significant fluid circulation along major tectonic contacts between basement and sedimentary cover during Alpine convergence.

INTRODUCTION

World-class Pb–Zn–Ag deposits are commonly associated with fluid circulation at basement/cover unconformities in extensive basins (Boiron et al., 2010). However, less-common Pb–Zn–Ag deposits may have an extended evolution influenced by orogenic processes (Williams, 1998) that redistributed the ore minerals (Cugerone et al., 2021). Extracting the ages of crystallization and subsequent remobilization of polymetallic ore deposits has proven challenging due to potential reopening of the isotopic systems (Chiaradia, 2023). Dating actinide-rich accessory minerals is the most common and reliable method for obtaining accurate ages because of the possibility to check for concordance using the triple U–Th–Pb decay series (Rasmussen et al., 2006; Li et al., 2019). However, that approach has limitations due to the relative scarcity and small size of accessory minerals suitable for dating (Engi, 2017). The recent development of in situ Rb–Sr dating (Zack and Hogmalm, 2016) on ubiquitous and abundant minerals (e.g., mica, feldspar, apatite) has opened new avenues for constraining the age of deposits as young as 28.1 ± 2.2 Ma (Şengün et al., 2019). The Rb–Sr method can assess not only the primary age but also subsequent periods of mineralization (Olierook et al., 2020; Tillberg et al., 2021). Proterozoic Rb–Sr ages preserved within Caledonian ore bodies imply inheritance and remobilization during the subsequent orogenic stages (Tillberg et al., 2021).

Our study investigates the timing and tempo of Pb–Zn–Ag mineralization along a lithostructural profile in the Western Alps in France, where the tectonic and metamorphic evolution and fluid circulation are well constrained (Handy et al., 2010; Gnos et al., 2021). The abundance of Pb–Zn–Ag mineralization in this area has been attributed to Variscan orogenesis, Mesozoic Tethyan opening, or Alpine remobilization (Nägler et al., 1995). However, recent in situ U–Pb dating by Bertauts et al. (2022) of stratabound Pb–Zn–Ag deposits at Mâcot-la Plagne and

46   Peisey-Nancroix (southeastern France) suggests a new Alpine orogenic period of metallization.

47   To consolidate these results, we used a multi-system approach involving in situ U–Th–Pb and Rb–

48   Sr dating to compare and constrain ages.

49

50   **GEOLOGY AND SAMPLING**

51   Samples were collected along an east-west transect from the Briançonnais domain of the

52   internal Alps to the Belledonne external crystalline massif (Fig. 1). The Briançonnais domain

53   corresponds to the European continental margin and consists of Variscan basement comprising

54   Carboniferous schists and locally some Mesozoic sediments. It was partially subducted under the

55   African tectonic plate before being thrust over the European tectonic plate during the Cenozoic

56   Alpine convergence (Handy et al., 2010). The sedimentary cover is characterized by low-

57   temperature metamorphism (<500 °C) and intense deformation (Strzerzynski et al., 2012). The

58   Belledonne massif is composed of Variscan basement rocks of the European plate, which

59   underwent lower greenschist facies metamorphism and only localized deformation during the

60   Alpine collision (Rossi et al., 2005). The internal metamorphic Alps are separated from the

61   external Alps by the Penninic front, which marks the onset of the European margin collision at ca.

62   35 Ma (Ceriani et al., 2001).

63   We collected 44 samples from mine tailings of seven historic Pb–Zn–Ag deposits. Of these,

64   only four samples from two different lithostructural contexts contain accessory allanite and

65   monazite suitable for U–Th–Pb dating. In the internal Briançonnais domain, one sample from the

66   Peisey-Nancroix deposit is located within the deformed Permian–Triassic cover along the Internal

67   Briançonnais fault (IBF; Fig. 1). In the Belledonne massif, the three samples come from the

68   subsidiary Pb–Zn–Ag mineralization of the Penay and Le Gros Villan deposits, which are located

69   in sub-vertical northeast-southwest dextral shear zones along major faults separating the massif

70   from the Mesozoic cover (Fig. 1).
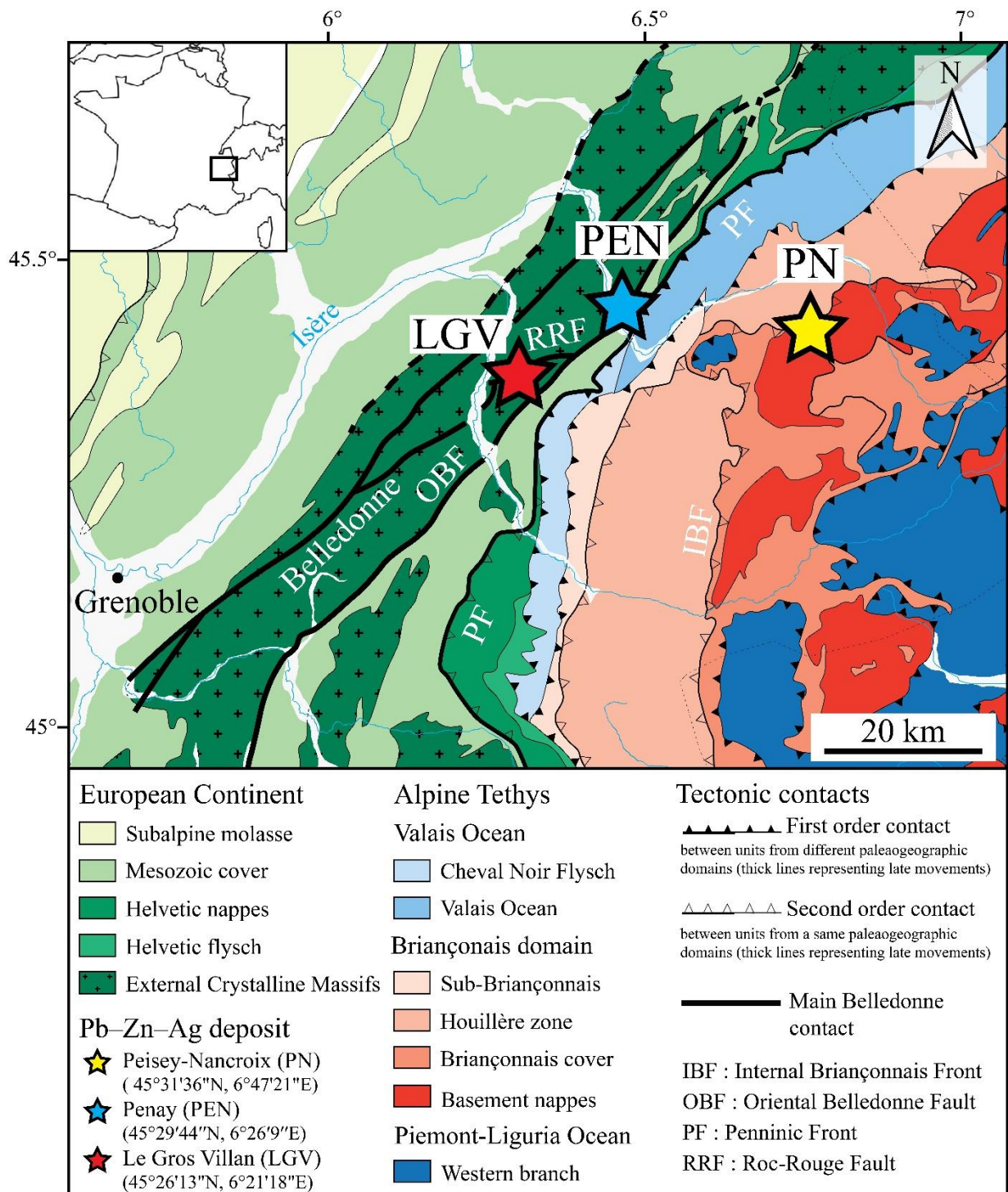
Figure 1. Location of the studied Pb–Zn–Ag mineralizations on the tectonic map of the Western Alps (northern French Alps), modified from Bousquet et al. (2012).

RESULTS

Mineralogy and Microstructures

The Pb–Zn–Ag mineralization consists mainly of galena with variable amounts of chalcopyrite, sphalerite, tetrahedrite-tennantite, and pyrite. The four samples show evidence of a high-strain regime with clasts hosted in a fine-grained equigranular recrystallized matrix.

Based on mineralogy and microstructures (Bertauts et al., 2022), mineralization in the Peisey-Nancroix deposit appears to be synchronous with dynamic quartz recrystallization associated with the precipitation of phengite (Fig. 2A) and monazite (Fig. 2B). The Penay sample shows massive sphalerite in a galena-sphalerite matrix. Clasts of albite, quartz, and foliated phengite aggregates are found within the massive sphalerite and recrystallized matrix (Fig. 2C). Subhedral to anhedral allanite grains are intergrown with sulfides (galena and sphalerite) and phengite contains inclusions of these minerals, indicating a common origin (Fig. 2D). The Le Gros Villan mineralization consists of centimeter-long galena-chalcopyrite-sphalerite-quartz veins hosted in a matrix of recrystallized, partially sericitized quartz and K-feldspar clasts. Phengite that formed at this stage is referred to herein as Ph1. Fractures within the K-feldspar clasts are filled by sulfides (galena and chalcopyrite). Monazite occurs as inclusions within other minerals and forms part of intergrowths with sulfides (Fig. 2F). Hourglass sector zoning within the monazite indicates a single crystallization stage during primary mineralization. The primary mineralization is affected by a second stage of deformation and recrystallization expressed by a foliation made of phengite (Ph2) and secondary fine-grained foliated galena (Gn2) that in places cuts the primary sulfides (Fig. 2E). In these foliated domains, the shape of monazite grains is controlled by foliation deflection of oriented acicular phengite grains.
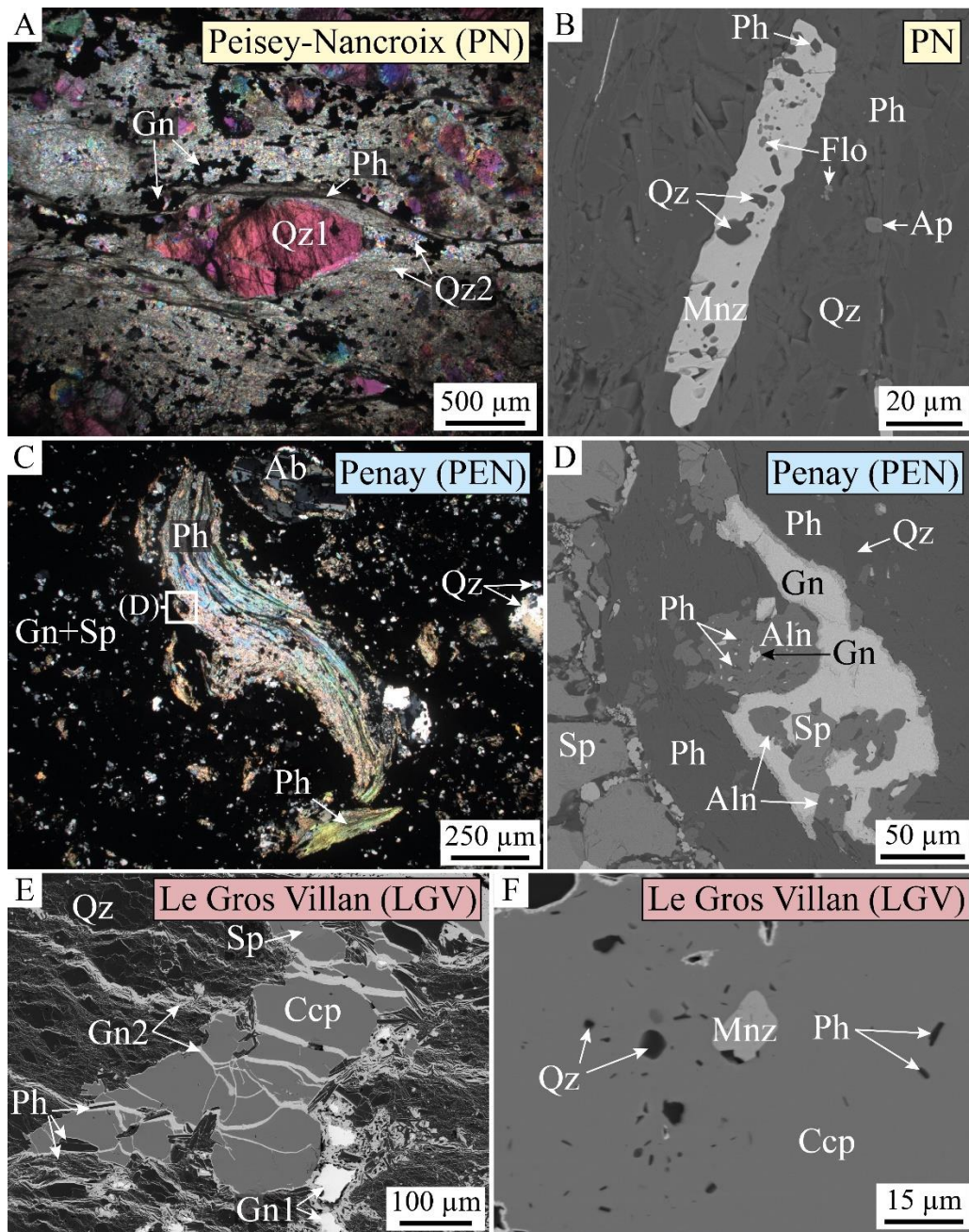
Figure 2. Examples of analyzed phengite (A, C, E) and accessory minerals (B, D, F) used for dating, observed using optical (A, C) and backscattered electron (B, D, E, F) microscopy. The two Peisey-Nancroix samples show: (A) deformed quartz (Qz) Qz1 porphyroclasts shaped by micrometric phengite (Ph) oriented in the foliation, sulfides, and equigranular micrograins of Qz2 (thick section, polarized light) (Gn—galena); and (B) prismatic monazite (Mnz) grain with a poikilitic texture highlighted by quartz, spherical florencite (Flo), and acicular phengite inclusions (Ap—apatite). The massive sulfides from thin sections of Penay show: (C) porphyroclasts of a foliated phengite foliated and folded, albite (Ab), and quartz hosted in a sphalerite-galena matrix (Gn + Sp); and (D) intergrowth texture between galena, sphalerite, and anhedral allanite (Aln) grains within the foliated phengite clast. The sample from Le Gros Villan shows: (E) chalcopyrite (Ccp) cracks filled by oriented acicular phengite and Gn2 crystallization; and (F) subhedral monazite inclusion within chalcopyrite. Abbreviations from Warr (2021).

94   Electron microprobe point analysis and X-ray mapping demonstrated that phengite from

95   the three deposits have homogeneous major and minor element compositions (Table S1 and Figs.

96   S1 and S2 in the Supplemental Material1).

97

98   **In situ LA-ICP-MS Rb–Sr and U–Th–Pb Dating**

99   The U–Pb analyses on 26 monazite grains from the Peisey-Nancroix deposit (Fig. 3A;

100   Table S5) define an isochron in the Tera-Wasserburg diagram that intersects the Concordia at 35.1

101   ± 0.6 Ma (Bertauts et al., 2022). This age is similar to that obtained on 52 in situ Rb–Sr isotopic

102   analyses on five phengite crystal aggregates (Table S8) showing 87Rb/86Sr values ranging from

103   350 to 800, aligned along an array with a slope corresponding to an age of 34.6 ± 4.7 Ma with an

104   initial 87Sr/86Sr value of 0.771 ± 0.034. Two spots have higher Sr contents and Rb/Sr values <70,

105   which could correspond to phengite with higher Sr contents or inclusions of Sr-rich minerals such

106   as apatite. When these two spots are added, the resulting isochron gives an older age of 40.1 ± 3.2

107   Ma with an initial Sr isotope ratio of 0.724 ± 0.014 (Fig. 3B).

108   The Th–Pb analyses of allanite from the Penay deposit (Table S7) are plotted in an isochron

109   diagram 208Pb/206Pbc (c—common) versus 232Th/206Pbc (n = 10, Fig. 3C). The regression

110   yields a Th/Pb age for allanite of 14.9 ± 7.6 Ma. In situ Rb–Sr isotope analyses of three Penay

111   phengite aggregates located within massive sphalerite or fine-grained galena-sphalerite matrix

112   (Table S8) define an isochron age of 18.4 ± 7.2 Ma (n = 35) with an initial 87Sr/86Sr value of

113   0.7214 ± 0.0065 consistent with the Th–Pb age. Six analyses of co-genetic albite grains yield a

114   scattered Sr-isotope weighted mean of 0.7213 ± 0.0030. When included in the regression, the age

115   remains the same, but the uncertainty of the isochron regression decreases to 3.6 Ma (Fig. 3D).
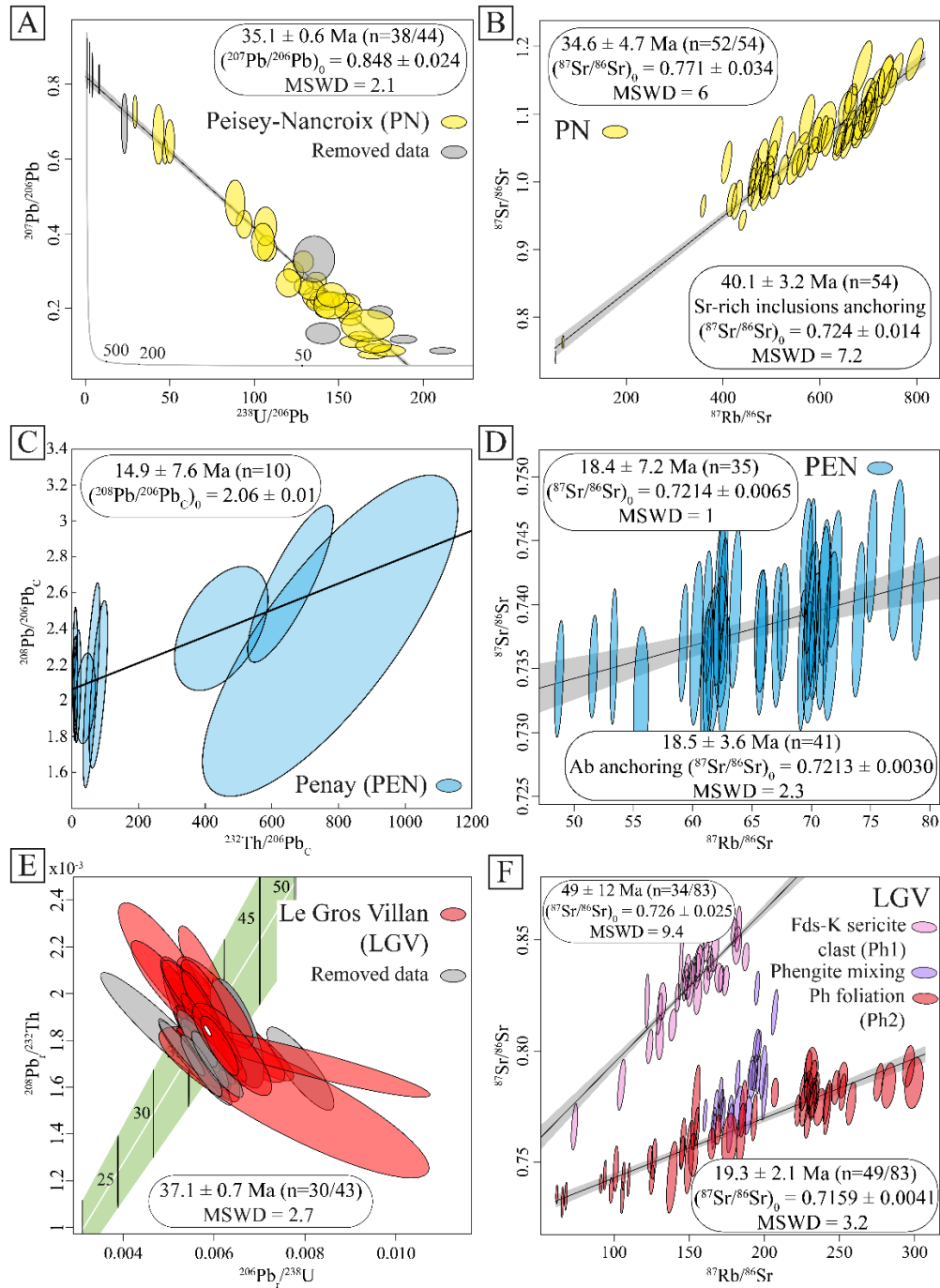
Figure 3. U–Pb (A, C, E) and Rb–Sr (B, D, F) laser ablation–inductively coupled plasma–mass spectrometry analyses on rare earth element–rich phases and phengite (Ph), respectively, for the Peisey-Nancroix (PN) (A, B), Penay (PEN) (C, D) and Le Gros Villan (LGV) (E, F) mineralizations. (A) Tera-Wasserburg diagram of PN monazite without any correction from Bertauts et al. (2022). (C) 206Pbc normalized Th–Pb isochron of PEN allanite. (E) U–Th–Pb data from LGV monazite are plotted on a 208Pbr/232Th versus 206Pbr/238U Concordia diagram using the total Pb/U–Th algorithm of Vermeesch (2020). Rb–Sr isochrons and calculated ages for (B) PN sample; (D) PEN sample (Ab—albite); and (F) LGV sample. Fds-K—K-feldspar. Data ellipses represent 2σ errors. MSWD—mean square of weighted deviates.

116   The U–Th–Pb monazite dating from the Le Gros Villan deposit was performed on 22

117   monazite grains obtained from two different thin sections (Table S6). After common Pb correction

118   for the three Pb isotopes (206Pb, 207Pb, and 208Pb), the monazite data yield a Concordia age of

119   37.1 ± 0.7 Ma (n = 30/43) on a 208Pbr/232Th (r—radiogenic) versus 206Pbr/238U diagram (Fig.

120   3E). Furthermore, Rb–Sr isotopic analyses were also performed on 10 phengite clusters (Table S8)

121   within sericitized feldspar (Ph1) or secondary foliation (Ph2). All data from the Ph2 foliation align

122   along an isochron that yields an age of 19.3 ± 2.1 Ma. In comparison, the Ph1 results are more

123   complex to interpret, but phengites in one clast plot on a Rb–Sr linear array give an age of 49 ± 12

124   Ma, overlapping the U–Th–Pb age. The other analyses plot between the two isochrons between

125   ca. 49 and 19 Ma (Fig. 3F).

126

127   **DISCUSSION**

128   **Strenght of U–Th–Pb and Rb–Sr Geochronology**

129   In fluid-rich environments, the Rb–Sr isochron ages are generally recording the phengite

130   crystallization age (Glodny et al., 2008; Villa, 2016). To prepare the groundwork for in situ dating,

131   careful mineralogical and microstructural relationships were established to determine the

132   crystallization sequences. Homogeneous major and minor elements compositions of phengite are

133   interpreted as one phengite population without recrystallizations (Fig. S1 and Fig. S2). Intergrowth

134   and inclusion relationships (Fig. 2), as well as mineral zoning, indicate that the phengite and REE-

135   minerals are cogenetic. Except Ph2 from the Le Gros-Villan, they coincide with the main stage of

136   sulfide precipitation and thus record the primary age of the Pb–Zn–Ag deposits. Indeed, there is

137   equilibration of the two isotopic systems (Rb–Sr and U–Th–Pb) giving consistent Alpine ages

138   (Fig. 3). Even in the more complex case of the Le Gros Villan deposit, the primary phengite (Ph1)

139   which corresponds to sericitization of K-feldspar, has scattered Rb–Sr isotopic analyses but with

140   a discrete alignment at 49 ± 12 Ma. This older age overlaps with the U–Th–Pb age of the monazite

141   (37.1 ± 0.7 Ma) attributed to the primary mineralization (Fig. 2E, F), with probably some

142   inheritance from K-feldspar. Such results clearly demonstrate the strength of the in situ method

143   used here, because mixing between incompletely reset mica and/or K-feldspar domains has been

144   a recurring problem in solution-based studies (e.g., Müller et al., 1999; Bröcker et al., 2013).

145   The U–Th–Pb dating was complicated by two factors: (i) the scarcity and small size of

146   mineral grains suitable for dating, with only 3 samples out of 44 yielding suitable material, and (2)

147   the possible incorporation of common Pb in this Pb-rich environment, as seen for the Le Gros

148   Villan monazite and, more importantly, for the Penay allanite. In contrast, the ubiquity of mica,

149   the structural control of this mineral, and minimal sample preparation, are advantages of the Rb–

150   Sr system when used for dating of orogenic mineralization. With a wide range of Rb/Sr ratios, in

151   situ dating of white mica can yield a well-resolved Alpine age of 19.3 Ma ± 2.1 Ma for the Le

152   Gros Villan deposit without isochron anchoring by other phases (10% precision). For samples with

153   lower Rb/Sr spreading (40% precision), isochron anchoring with co-genetic Sr-rich phases

154   improves the precision by about 20%. For samples from the Peisey-Nancroix deposit, isochron

155   anchoring modifies the initial $^{87}Sr/^{86}Sr$ value and thus the calculated age, but within the range of

156   uncertainties (40.1 Ma ± 3.2 Ma instead of 34.6 ± 4.7 Ma). The Rb/Sr calibration on the Mica-Mg

157   nano-powder (Tab. S9) may induce a few percent drifted phengite age, but this would represent

158   less than 1 Ma for such young deposit within the uncertainty.

159   Another advantage of cross-comparison of Rb–Sr and U–Th–Pb dating paired in thin

160   section is the ability to distinguish different crystallization stages (Chiaradia, 2023). The primary

161   Eocene mineralization of the Le Gros Villan deposit (37.1 ± 0.7 Ma, monazite) contains secondary

162   phengite (Ph2) and galena (Gn2) in post-mineralization microstructures (localized foliation and

163   fractures, Fig. 2E). Thus, Ph2 in this deposit is thought to record secondary Miocene

164   remobilization at 19.3 ± 2.1 Ma during deformation. In this case, two Rb–Sr ages correspond to

165   two distinct microstructures (Fig. 3).

166

167   **Evidence of Alpine Mineralization and Remobilization**

168   In Peisey-Nancroix, one of the two largest historical Pb–Zn–Ag deposits from the French

169   Alps, the new Rb–Sr dating (Fig. 3B) is consistent with the well-resolved U–Pb syn-orogenic

170   Alpine ages from Bertauts et al. (2022), ruling out a possible sedimentary-diagenetic origin or

171   inheritance for these deposits despite their presence in Triassic quartzite (Rogel, 1961). The

172   deposits formed over a short period of time, which was less than the analytical resolution of in situ

173   U–Pb dating (35.1 ± 0.6 Ma) and Rb–Sr dating (35–40 Ma). The age of ca. 35 Ma is attributed to

174   fluid circulation coeval with the major top-to-west thrusting within the Penninic front (and the

175   Internal Briançonnais front) at the onset of the collision (Strzerzynski et al., 2012).

176   The two deposits in the external crystalline massifs are located in the Variscan basement

177   and show evidence of sulfide recrystallization, suggesting episodic growth and/or remobilization.

178   However, neither in situ U–Th–Pb dating of REE-rich phases nor Rb–Sr dating of white mica

179   indicate a pre-Alpine age. The Miocene ages (15–20 Ma) obtained in these deposits could

180   correspond to the circulation of non-mineralizing fluids (Rolland and Rossi, 2016). The new Late

181   Eocene U–Th–Pb monazite ages in the Le Gros Villan mineralization (Fig. 3E) document early,

182   previously undocumented fluid circulation and are more comparable to those obtained in the

183   internal domains (Gnos et al., 2021). In the external domains, sedimentation had started in a

184   flexural basin, and thrusting in the internal domain along the Penninic front had just begun (Simon-

185 Labric et al., 2009). Thus, early mineralization in the Belledonne massif basement may have been

186 promoted by fluid circulation in Variscan-inherited structures reactivated during burial of the

187 massif (Guillot and Ménot, 2009).

188

189 **CONCLUSIONS**

190 Concordance of the paired in situ Rb–Sr and U–Th–Pb ages in the Western Alps suggests

191 that these isotopic systems reached equilibrium during hydrothermal Pb–Zn–Ag mineralization.

192 The combination of Rb–Sr and U–Th–Pb systems unambiguously indicates Alpine ages for these

193 Pb–Zn–Ag deposits. Two ages, 35–40 Ma and 15–20 Ma, are associated with collision and

194 exhumation of the Belledonne massif. The Rb–Sr geochronological data set obtained on texturally

195 distinctive micas provides evidence for episodic evolution of Alpine Pb–Zn–Ag mineralization.

196 The Pb–Zn–Ag mineralization was produced by fluid circulation along major lithostructural

197 contacts during the Alpine collision.

198

216 **REFERENCES CITED**

217 Bertauts, M., Janots, E., Rossi, M., Duhamel-Achin, I., Boiron, M.-C., Airaghi, L., Lanari, P.,
218   Lach, P., Peiffert, C., and Magnin, V., 2022, A New Alpine Metallogenic Model for the
219   Pb-Ag Orogenic Deposits of Macôt-la Plagne and Peisey-Nancroix (Western Alps,
220   France): Geosciences, v. 12, p. 331, https://doi.org/10.3390/geosciences12090331.

221 Boiron, M.-C., Cathelineau, M., and Richard, A., 2010, Fluid flows and metal deposition near
222   basement /cover unconformity: lessons and analogies from Pb-Zn-F-Ba systems for the
223   understanding of Proterozoic U deposits: Geofluids, v. 10, p. 270–292,
224   https://doi.org/10.1111/j.1468-8123.2010.00289.x.

225 Bousquet, R., Schmid, S.M., Zeilinger, G., Oberhänsli, R., Rosenberg, C., Molli, G., Robert, C.,
226   Wiederkehr, M., and Rossi, P., 2012, Tectonic framework of the Alps: Commission for the
227   geological map of the world (www.geodynalps.org).

228 Bröcker, M., Baldwin, S., and Arkudas, R., 2013, The geological significance of 40Ar/ 39Ar and
229   Rb-Sr white mica ages from Syros and Sifnos, Greece: a record of continuous
230   (re)crystallization during exhumation? Journal of Metamorphic Geology, v. 31, p. 629–
231   646, https://doi.org/10.1111/jmg.12037.

232 Ceriani, S., Fügenschuh, B., and Schmid, S.M., 2001, Multi-stage thrusting at the "Penninic Front"
233   in the Western Alps between Mont Blanc and Pelvoux massifs: International Journal of
234   Earth Sciences, v. 90, p. 685–702, https://doi.org/10.1007/s005310000188.

235 Chiaradia, M., 2023, Radiometric Dating Applied to Ore Deposits: Theory and Methods, *in*
236   Huston, D. and Gutzmer, J. eds., Isotopes in Economic Geology, Metallogenesis and
237   Exploration, Cham, Springer International Publishing, Mineral Resource Reviews, p. 15–
238   35, https://doi.org/10.1007/978-3-031-27897-6_2.

239 Cugerone, A., Cenki-Tok, B., Muñoz, M., Kouzmanov, K., Oliot, E., Motto-Ros, V., and Le Goff,
240   E., 2021, Behavior of critical metals in metamorphosed Pb-Zn ore deposits: example from
241   the Pyrenean Axial Zone: Mineralium Deposita, v. 56, p. 685–705,
242   https://doi.org/10.1007/s00126-020-01000-9.

243 Engi, M., 2017, Petrochronology Based on REE-Minerals: Monazite, Allanite, Xenotime, Apatite:
244   Reviews in Mineralogy and Geochemistry, v. 83, p. 365–418,
245   https://doi.org/10.2138/rmg.2017.83.12.

246 Glodny, J., Kühn, A., and Austrheim, H., 2008, Diffusion versus recrystallization processes in Rb–
247   Sr geochronology: Isotopic relics in eclogite facies rocks, Western Gneiss Region, Norway:
248   Geochimica et Cosmochimica Acta, v. 72, p. 506–525,
249   https://doi.org/10.1016/j.gca.2007.10.021.

250 Gnos, E., Mullis, J., Ricchi, E., Bergemann, C.A., Janots, E., and Berger, A., 2021, Episodes of
251   fissure formation in the Alps: connecting quartz fluid inclusion, fissure monazite age, and
252   fissure orientation data: Swiss Journal of Geosciences, v. 114, p. 14,
253   https://doi.org/10.1186/s00015-021-00391-9.

254 Guillot, S., and Ménot, R.-P., 2009, Paleozoic evolution of the External Crystalline Massifs of the
255   Western Alps: Comptes Rendus Geoscience, v. 341, p. 253–265,
256   https://doi.org/10.1016/j.crte.2008.11.010.

257 Handy, M.R., M. Schmid, S., Bousquet, R., Kissling, E., and Bernoulli, D., 2010, Reconciling
258   plate-tectonic reconstructions of Alpine Tethys with the geological–geophysical record of

259   spreading and subduction in the Alps: Earth-Science Reviews, v. 102, p. 121–158,
260   https://doi.org/10.1016/j.earscirev.2010.06.002.

261   Li, L.-X., Zi, J.-W., Li, H.-M., Rasmussen, B., Wilde, S.A., Sheppard, S., Ma, Y.-B., Meng, J.,
262   and Song, Z., 2019, High-Grade Magnetite Mineralization at 1.86 Ga in Neoarchean
263   Banded Iron Formations, Gongchangling, China: In Situ U-Pb Geochronology of
264   Metamorphic-Hydrothermal Zircon and Monazite: Economic Geology, v. 114, p. 1159–
265   1175, https://doi.org/10.5382/econgeo.4678.

266   Müller, W., Dallmeyer, R.D., Neubauer, F., and Thöni, M., 1999, Deformation-induced resetting
267   of Rb/Sr and 40Ar/39Ar mineral systems in a low-grade, polymetamorphic terrane (Eastern
268   Alps, Austria): Journal of the Geological Society, v. 156, p. 261–278,
269   https://doi.org/10.1144/gsjgs.156.2.0261.

270   Nägler, Th.F., Pettke, Th., and Marshall, D., 1995, Initial isotopic heterogeneity and secondary
271   disturbance of the Sm-Nd system in fluorites and fluid inclusions: A study on mesothermal
272   veins from the central and western Swiss Alps: Chemical Geology, v. 125, p. 241–248,
273   https://doi.org/10.1016/0009-2541(95)00091-Y.

274   Olierook, H.K.H. et al., 2020, Resolving multiple geological events using in situ Rb–Sr
275   geochronology: implications for metallogenesis at Tropicana, Western Australia:
276   Geochronology, v. 2, p. 283–303, https://doi.org/10.5194/gchron-2-283-2020.

277   Rasmussen, B., Sheppard, S., and Fletcher, I.R., 2006, Testing ore deposit models using in situ U-
278   Pb geochronology of hydrothermal monazite: Paleoproterozoic gold mineralization in
279   northern Australia: Geology, v. 34, p. 77, https://doi.org/10.1130/G22058.1.

280   Rogel, P., 1961, Le gisement de Plomb de La Plagne (Savoie). Etude géologique et métallogénique
281   [Thèse de 3e cycle]: Faculté des sciences de l'université de Paris, 74 p.

282   Rolland, Y., and Rossi, M., 2016, Two-stage fluid flow and element transfers in shear zones during
283   collision burial-exhumation cycle: Insights from the Mont Blanc Crystalline Massif
284   (Western Alps): Journal of Geodynamics, v. 101, p. 88–108,
285   https://doi.org/10.1016/j.jog.2016.03.016.

286 Rossi, M., Rolland, Y., Vidal, O., and Cox, S.F., 2005, Geochemical variations and element
287   transfer during shear-zone development and related episyenites at middle crust depths:
288   insights from the Mont Blanc granite (French — Italian Alps): Geological Society, London,
289   Special Publications, v. 245, p. 373–396, https://doi.org/10.1144/GSL.SP.2005.245.01.18.

290 Şengün, F., Erlandsson, V.B., Hogmalm, J., and Zack, T., 2019, In situ Rb-Sr dating of K-bearing
291   minerals from the orogenic Akçaabat gold deposit in the Menderes Massif, Western
292   Anatolia, Turkey: Journal of Asian Earth Sciences, v. 185, p. 104048,
293   https://doi.org/10.1016/j.jseaes.2019.104048.

294 Simon-Labric, T., Rolland, Y., Dumont, T., Heymes, T., Authemayou, C., Corsini, M., and
295   Fornari, M., 2009, 40Ar/39Ar dating of Penninic Front tectonic displacement (W Alps)
296   during the Lower Oligocene (31-34 Ma): Terra Nova, v. 21, p. 127–136,
297   https://doi.org/10.1111/j.1365-3121.2009.00865.x.

298 Strzerzynski, P., Guillot, S., Leloup, P.H., Arnaud, N., Vidal, O., Ledru, P., Courrioux, G., and
299   Darmendrail, X., 2012, Tectono-metamorphic evolution of the Briançonnais zone
300   (Modane-Aussois and Southern Vanoise units, Lyon Turin transect, Western Alps): Journal
301   of Geodynamics, v. 56–57, p. 55–75, https://doi.org/10.1016/j.jog.2011.11.010.

302 Tillberg, M., Drake, H., Zack, T., Hogmalm, J., Kooijman, E., and Åström, M., 2021,
303   Reconstructing craton-scale tectonic events via in situ Rb-Sr geochronology of poly-
304   phased vein mineralization: Terra Nova, v. 33, p. 502–510,
305   https://doi.org/10.1111/ter.12542.

306 Vermeesch, P., 2020, Unifying the U–Pb and Th–Pb methods: joint isochron regression and
307   common Pb correction: Geochronology, v. 2, p. 119–131, https://doi.org/10.5194/gchron-
308   2-119-2020.

309 Villa, I.M., 2016, Diffusion in mineral geochronometers: Present and absent: Chemical Geology,
310   v. 420, p. 1–10, https://doi.org/10.1016/j.chemgeo.2015.11.001.

311 Warr, L.N., 2021, IMA–CNMNC approved mineral symbols: Mineralogical Magazine, v. 85, p.
312   291–320, https://doi.org/10.1180/mgm.2021.43.

313 Williams, P.J., 1998, Metalliferous economic geology of the Mt Isa Eastern Succession,
314   Queensland: Australian Journal of Earth Sciences, v. 45, p. 329–341,
315   https://doi.org/10.1080/08120099808728395.

316 Zack, T., and Hogmalm, K.J., 2016, Laser ablation Rb/Sr dating by online chemical separation of
317   Rb and Sr in an oxygen-filled reaction cell: Chemical Geology, v. 437, p. 120–133,
318   https://doi.org/10.1016/j.chemgeo.2016.05.027.

319

320 [1]Supplemental Material. Analytical methods and monazite U–Th–Pb, allanite Th–Pb, and phengite

321 Rb–Sr data analysis for the Pb–Zn–Ag deposits in the French Northern Alps; chemical map with

322 summary table of the phengite and albite compositions; Tables S1–S8; and Figures S1 and S2.

323 Please visit https://doi .org /10 .1130 /GEOL .S.25209137 to access the supplemental material;

324 contact editing@geosociety.org with any questions.